Lars Schumacher and Rainer Pöttgen*

Aluminum-rich cage compounds AT_2Al_{20} (A = Sr, Eu; T = Ti, V)

https://doi.org/10.1515/zkri-2025-0039
Received August 5, 2025; accepted September 17, 2025;
published online October 16, 2025

Abstract: The $CeCr_2Al_{20}$-type (space group $Fd\bar{3}m$) aluminum-rich intermetallic compounds AT_2Al_{20} (A = Sr, Eu; T = Ti, V) were synthesized from the elements in alumina crucibles within evacuated sealed silica ampoules and characterized through X-ray powder patterns. $SrTi_2Al_{20}$ (a = 1,475.25(6) pm) and SrV_2Al_{20} (a = 1,459.81(8) pm) are the first strontium-based aluminides with $CeCr_2Al_{20}$-type structure. The structures of $Sr_{0.836(2)}V_2Al_{20}$, $Sr_{0.961(1)}V_2Al_{20}$ and $Eu_{0.964(2)}V_2Al_{20}$ were refined from single crystal X-ray diffractometer data. Refinements of the occupancy parameters revealed defect formation on the 8a sites. In the strontium series, the lattice parameter scales with the occupancy parameter. Temperature dependent magnetic susceptibility data for the $SrTi_2Al_{20}$ and SrV_2Al_{20} samples show diamagnetic and Pauli paramagnetic behavior, respectively.

Keywords: cage compounds; intermetallics; crystal structure; Pauli paramagnetism; diamagnetism

1 Introduction

Among the intermetallic cage compounds, the structural families of the clathrates,[1] the Remeika phases[2,3] and the family of $CeCr_2Al_{20}$-type intermetallic compounds[4,5] play an important role. They have thoroughly been investigated with respect to their broadly varying chemical and physical properties; the clathrates and Remeika phases in particular for their thermoelectric behavior.

The $CeCr_2Al_{20}$-type family of compounds meanwhile has more than 340 entries in the Pearson data base.[6] This structure type shows an extreme flexibility regarding the chemical composition as well as the valence electron count. The rare earth site can be substituted by calcium or strontium, transition metals from the titanium to the copper group have been used and besides aluminides, magnesium, zinc (additionally with partial substitution by indium or tin), cadmium and gallium containing representatives have been reported. These substitutions allow for the broad range of the valence electron count (VEC). The extreme values are 59 for the $RERu_2Zn_{20}$ series and 76 for $ThMo_2Al_{20}$.

Recent research on $CeCr_2Al_{20}$-type compounds mainly focused on elucidating the existence ranges by variation of the composition on all three substructures. $ZrCu_2Zn_{20}$,[7] $HfCu_2Zn_{20}$ and $NbCu_2Zn_{20}$[8] are the so far only representatives with copper on the chromium substructure of the prototype and $HfMn_2Zn_{20}$[9] is among the few manganese containing representatives. An interesting extension of the $CeCr_2Al_{20}$-type structural family was observed for the aluminides $RETi_2Al_{20}$ (RE = Eu, Gd, Tb, Dy and Yb) which show the formation of solid solutions $RETi_2Al_{20-x}Ga_x$ with gallium in the ranges $0 \le x \le 10$.[10] Thus, at least aluminum-gallium mixing is possible.

When completing the $RERh_2Cd_{20}$ series of compounds,[11] we obtained divalent $EuRh_2Cd_{20}$ and isotypic $SrRh_2Cd_{20}$, the first strontium representative with $CeCr_2Al_{20}$-type structure. This is understandable given that the radii for coordination number 6[12] for Eu^{2+} (117 pm) and Sr^{2+} (118 pm) are almost similar. In continuation of our structural and ^{151}Eu Mössbauer spectroscopic studies on the EuT_2Al_{20}[13] and EuT_2Cd_{20}[11] intermetallics, we have systematically searched for the strontium analogs to the europium phases. Herein we report on the synthesis and structural characterization of $SrTi_2Al_{20}$ and SrV_2Al_{20}, the strontium analogs to $EuTi_2Al_{20}$[14,15] and EuV_2Al_{20}.[16–19]

2 Experimental

2.1 Syntheses

For the synthesis of the samples, pieces of strontium (Onyxmet, 99.95 %), europium (Onyxmet, 99.99 %), titanium (Koch light, 99.9 %), vanadium (Alfa Aesar; 99.7 %) and aluminum (Koch Chemicals, 99.99 %) were used. The surface of the moisture sensitive elements strontium and europium were cleaned mechanically under dry cyclohexane (dried over sodium wire) and stored under dry argon (Westfalen, 99.998 %, purified by using titanium sponge (T = 873 K), silica

***Corresponding author: Rainer Pöttgen**, Institut für Anorganische und Analytische Chemie, Universität Münster, Corrensstrasse 30, 48149, Münster, Germany, E-mail: pottgen@uni-muenster.de
Lars Schumacher, Institut für Anorganische und Analytische Chemie, Universität Münster, Corrensstrasse 30, 48149, Münster, Germany

gel and molecular sieves) until use. The elements were weighed in the ideal atomic ratios and placed in aluminum oxide crucibles. These were sealed in evacuated silica ampoules (oxidation protection), placed in a muffle furnace and heated to 1123 K for 300 h. Afterwards, the samples were cooled to room temperature at a rate of 6 K h^{-1}. Since the single crystal data (*vide infra*) revealed small defects on the 8*a* strontium site, an additional sample with a slight excess of Sr (starting composition $Sr_{1.2}V_2Al_{20}$) was prepared under the same annealing conditions. The reaction ampoules were then broken and the alumina crucibles with the products were placed in beakers with 1 M hydrochloric acid. Since at least at the beginning of the reactions, the syntheses were run under self-flux conditions,[20] residual aluminum remained between the product grain boundaries. After the hydrochloric acid treatment, the product was recovered by decantation and washed with demineralized water. The remaining samples showed a metallic luster and were stable in air over months.

2.2 X-ray diffraction

Pieces of the AT_2Al_{20} (A = Sr, Eu; T = Ti, V) samples were powdered in an agate mortar and characterized by powder X-ray diffraction at room temperature: Enraf-Nonius FR552 Guinier camera, Cu $K_{\alpha1}$ radiation, image plate system (Fujifilm, BAS-1800) and α-quartz (a = 491.30 and c = 540.46 pm) as an internal standard. The cubic lattice parameters (Table 1) were refined from the experimental 2θ values through a standard least-squares routine. The correct assignment of the *hkl* indices was ensured with parallel intensity calculations (Lazy Pulverix routine[21]).

Table 1: Lattice parameters (X-ray powder and single crystal data) of different SrT_2Al_{20} and $EuTAl_{20}$ (T = Ti, V) samples. Standard deviations are given in parentheses. P: powder data; SC: single crystal data. Data for the isotypic calcium compounds is given for comparison.

Compound	Source	a (pm)	V (nm^3)	Reference
$CaTi_2Al_{20}$	P	1,473.9(1)	3.2019	17
$SrTi_2Al_{20}$	P	1,475.25(6)	3.2109	This work
$EuTi_2Al_{20}$	P	1,472.26(5)	3.1912	13
$EuTi_2Al_{20}$	P	1,473.2(1)	3.1973	14
$EuTi_2Al_{20}$	P	1,477.85(3)	3.2277	15
CaV_2Al_{20}	P	1,458.7(2)	3.1038	16
SrV_2Al_{20}	P	1,459.81(8)	3.1109	This work
$Sr_{0.836(2)}V_2Al_{20}$	SC	1,459.90(9)	3.1115	This work
$Sr_{1.2}V_2Al_{20}$	P	1,464.36(6)	3.1401	This work
$Sr_{0.961(1)}V_2Al_{20}$	SC	1,464.11(4)	3.1385	This work
EuV_2Al_{20}	P	1,458.09(7)	3.0999	16
EuV_2Al_{20}	P	1,457.5(1)	3.0962	17
EuV_2Al_{20}	P	1,475.39(3)	3.2116	19
EuV_2Al_{20}	P	1,458.29(5)	3.1012	This work
$Eu_{0.964(2)}V_2Al_{20}$	SC	1,456.31(1)	3.0886	This work

Single crystals were selected from the carefully crushed vanadium-containing samples under an optical microscope and glued to thin quartz fibers using beeswax. The crystal quality was first checked through Laue photographs on a Buerger camera (white molybdenum radiation, image plate technique, Fujifilm, BAS-1800). The $Sr_{0.836(2)}V_2Al_{20}$ and $Sr_{0.961(1)}V_2Al_{20}$ data sets were measured at room temperature on a Stoe StadiVari (Mo microfocus source and a Pilatus detection system) diffractometer. The Gaussian-shaped profile of the microfocus X-ray source of the diffractometer required scaling along with the numerical absorption correction. A complete data set of the $Eu_{0.964(2)}V_2Al_{20}$ crystal was collected on a Bruker D8 Venture single-crystal diffractometer, equipped with a MoK_α microfocus source and a CCD detection system (PhotonIII CMOS). A numerical absorption correction was applied to the data set. Details of the data collections and the structure refinement data are summarized in Table 2.

2.3 Structure refinements

The three data sets showed high cubic Laue symmetry and the systematic extinctions were compatible with space group $Fd\bar{3}m$. The starting atomic parameters were obtained with the charge-flipping algorithm[22] implemented in Superflip[23] and the structures were refined on F^2 with the Jana2020 software package[24,25] with anisotropic displacement parameters for all sites. Separate refinement of the occupancy parameters showed defect formation on the 8*a* sites. These occupancies were refined as least-squares variable in the final cycles, leading to the compositions $Sr_{0.836(2)}V_2Al_{20}$, $Sr_{0.961(1)}V_2Al_{20}$ and $Eu_{0.964(2)}V_2Al_{20}$ for the studied crystals. The $Sr_{0.961(1)}V_2Al_{20}$ crystal showed reverse observe twinning (M = –1/3, 2/3, 2/3; 2/3, –1/3, 2/3; 2/3, 2/3; –1/3; spinel type interpenetration twins; 180° rotation around the threefold axis[26]) and a domain ratio of 0.969(2)/0.031. The final difference Fourier syntheses revealed no significant residual peaks. The refined atomic positions, displacement parameters and interatomic distances are given in Tables 3 and 4. Structural drawings were generated with Diamond 4.5[27] und edited with CorelDraw 24.3.[28]

CCDC–2478446 ($Sr_{0.836(2)}V_2Al_{20}$), CCDC–2478445 ($Sr_{0.961(1)}V_2Al_{20}$) and CCDC–2478447 ($Eu_{0.964(2)}V_2Al_{20}$) contain

Table 2: Crystal data and structure refinement parameters for $Sr_{0.836(2)}V_2Al_{20}$, $Sr_{0.961(1)}V_2Al_{20}$ and $Eu_{0.964(2)}V_2Al_{20}$; $CeCr_2Al_{20}$-type, space group $Fd\bar{3}m$ and Z = 8.

Refined composition	$Sr_{0.836(2)}V_2Al_{20}$	$Sr_{0.961(1)}V_2Al_{20}$	$Eu_{0.964(2)}V_2Al_{20}$
Formula weight, g mol^{-1}	714.9	725.7	778.0
Lattice parameter, pm (Single crystal data)	a = 1,459.90(9)	a = 1,464.11(4)	a = 1,456.31(1)
Unit cell volume, nm^3	3.1115	3.1385	3.0886
Diffractometer type	Stoe Stadivari	Stoe Stadivari	Bruker Venture
Calculated density, g cm^{-3}	3.05	3.07	3.39
Crystal size, µm	20 × 40 × 50	40 × 80 × 80	15 × 20 × 95
Transmission (min/max)	0.776/0.928	0.590/0.674	0.667/0.746
Detector distance, mm	40	40	50
Exposure time, s	30	20	35
Integr. param. (A, B, EMS)	7.0/−6.0/0.030	7.0/−6.0/0.030	–
Abs. coefficient, mm^{-1}	5.2	5.5	6.2
F(000), e	2,702	2,740	2,934
θ range, deg.	2.42–34.74	2.41–37.04	2.42–32.02
Range in hkl	±23/±23/±23	±24/±24/±24	±21/±21/±21
Total no. reflections	31,299	38,565	15,456
Independent refl./R_{int}	365/0.0683	609/0.0531	299/0.0327
Refl. with $I \geq 3\sigma(I)$/$R\sigma$	285/0.0151	547/0.0091	292/0.0069
Data/parameters	365/18	609/19	299/18
Goodness-of-fit on F^2	0.86	1.11	1.26
R/wR for $I > 3\sigma(I)$	0.0118/0.0282	0.0130/0.0324	0.0121/0.0300
R/wR for all data	0.0171/0.0288	0.0145/0.0325	0.0123/0.0300
Extinction coefficient	630(150)	4,500(200)	590(120)
Largest diff. peak/hole, e Å^{-3}	0.32/−0.25	0.34/−0.27	0.83/−0.37
Twin fraction	–	0.969(2)/0.031[a]	–

[a]M = −1/3, 2/3, 2/3; 2/3, −1/3, 2/3; 2/3, 2/3; −1/3.

the supplementary crystallographic data for this paper. These data can be obtained free of charge from The Cambridge Crystallographic Data Centre via www.ccdc.cam.ac.uk/data_request/cif.

2.4 Magnetic measurements

Crushed samples were filled in polypropylene capsules and mounted on a sample holder rod of a Dynacool PPMS (physical property measurement system) by Quantum Design using the VSM-option (vibrating sample magnetometer). The samples were investigated with $M(T)$ measurements in a temperature range of 2–300 K with different external fields (20 Oe and 10 kOe). Fitting and plotting was done using OriginPro 2024[29] and the graphical editing was done with CorelDraw 24.3.[28]

3 Results and discussion

3.1 Crystal chemistry

Within the family of $CeCr_2Al_{20}$-type phases, the series $RETi_2Al_{20}$ (RE = La–Nd, Sm, Eu–Yb)[14] and REV_2Al_{20} (RE = La–Nd, Sm, Eu–Dy)[4,16,17] have different existence ranges. The plots of the cell volumes (Iandelli plots)[17] of both series showed positive deviations for $EuTi_2Al_{20}$, $YbTi_2Al_{20}$ and EuV_2Al_{20}, indicating divalent ground states. This was corroborated through Curie-Weiss paramagnetism and long-range magnetic ordering in $EuTi_2Al_{20}$[15,17] and EuV_2Al_{20}[15,18] and Pauli paramagnetism in $YbTi_2Al_{20}$.[30]

Besides the pair Eu^{2+}/Sr^{2+} mentioned in the Introduction, also Yb^{2+} (102 pm) and Ca^{2+} (100 pm) have comparable radii.[12] Consequently, the isotypic CaT_2Al_{20} (T = Ti, V, Nb, Ta, Cr, Mo)[4,16,17] phases have been synthesized. During the present study we have now obtained the first strontium-based aluminides $SrTi_2Al_{20}$ and SrV_2Al_{20}.

Before exemplarily discussing the $Sr_{0.961(1)}V_2Al_{20}$ structure, we need to comment on the lattice parameters of the divalent ATi_2Al_{20} and AV_2Al_{20} representatives (Table 1). In the titanium series, the cell parameters follow the course of the radii in the sequence Ca→Eu→Sr; however, it is not clear why the $EuTi_2Al_{20}$ lattice parameter of 1,477.85(3) pm reported in ref. 15 is even larger than the one of $SrTi_2Al_{20}$. The situation for the vanadium-based samples is more complex. The single crystal data revealed defect formation on the 8a site and two crystals with compositions $Sr_{0.836(2)}V_2Al_{20}$ and $Sr_{0.961(1)}V_2Al_{20}$ were studied. Increasing strontium content leads to an increase of the lattice parameter. As an additional test, we also prepared a sample with a slight excess of strontium – 1.2Sr:2V:20Al as starting composition. The lattice parameter of this sample is only slightly larger than the one of $Sr_{0.961(1)}V_2Al_{20}$ and thus corresponds to the complete cage filling. Again, the lattice parameter reported for EuV_2Al_{20} in ref. 19 is substantially larger than that of $Sr_{0.961(1)}V_2Al_{20}$. This is not explainable. The CaV_2Al_{20} lattice parameter is very close to the one of EuV_2Al_{20}.

The strontium cations are the largest ones that form the $CeCr_2Al_{20}$-type phases. The representative with the largest unit cell parameter, however, is $LaPt_2Cd_{20}$ (1,573.9(5) pm)[31] and the one with the smallest is $NbNi_2Zn_{20}$ (1,380.9(1) pm).[32] Thus, besides the broad range in the VEC, the $CeCr_2Al_{20}$-type family also shows an enormous geometrical flexibility.

The partial occupancy of the 8a site is not a new feature. Defect formation was also observed for the series $Ce_{1-x}V_2Al_{20}$ and $Th_{1-x}V_2Al_{20}$ with an increasing lattice parameter towards x = 1.[33] The 8a site can also be partially occupied by gallium, however, the $Ga_xV_2Al_{20}$ series is limited to $0 \leq x \leq 0.6$

Table 3: Atomic coordinates and anisotropic displacement parameters (pm^2) for $Sr_{0.836(2)}V_2Al_{20}$, $Sr_{0.961(1)}V_2Al_{20}$ and $Eu_{0.964(2)}V_2Al_{20}$. The anisotropic displacement factor exponent takes the form: $-2\pi^2[(ha^*)^2U_{11} + \ldots + 2hka^*b^*U_{12}]$. U_{eq} is defined as one third of the trace of the orthogonalized U_{ij} tensor.

Atom	Wyck. Site	x	y	z	U_{11}	U_{22}	U_{33}	U_{12}	U_{13}	U_{23}	U_{eq}
$Sr_{0.836(2)}V_2Al_{20}$											
0.836(2)Sr	8*a*	1/8	1/8	1/8	162(1)	U_{11}	U_{11}	0	0	0	162(1)
V	16*d*	1/2	1/2	1/2	116(1)	U_{11}	U_{11}	−4(1)	U_{12}	U_{12}	116(1)
Al1	96 *g*	0.05883(2)	*x*	0.32559(2)	189(1)	U_{11}	151(2)	−38(1)	−6(1)	U_{13}	176(1)
Al2	48*f*	0.48627(3)	1/8	1/8	151(2)	147(2)	U_{22}	0	0	−24(2)	148(1)
Al3	16*c*	0	0	0	341(3)	U_{11}	U_{11}	12(3)	U_{12}	U_{12}	341(2)
$Sr_{0.961(1)}V_2Al_{20}$											
0.961(1)Sr	8*a*	1/8	1/8	1/8	131(1)	U_{11}	U_{11}	0	0	0	131(1)
V	16*d*	1/2	1/2	1/2	113(1)	U_{11}	U_{11}	−4(1)	U_{12}	U_{12}	113(1)
Al1	96*g*	0.05867(1)	*x*	0.32601(2)	184(1)	U_{11}	141(1)	−38(1)	−4(1)	U_{13}	170(1)
Al2	48*f*	0.48641(3)	1/8	1/8	147(1)	145(1)	U_{11}	0	0	−24(1)	145(1)
Al3	16*c*	0	0	0	298(2)	U_{11}	U_{11}	−57(2)	U_{12}	U_{12}	298(1)
$Eu_{0.964(2)}V_2Al_{20}$											
0.964(2)Eu	8*a*	1/8	1/8	1/8	79(1)	U_{11}	U_{11}	0	0	0	79(1)
V	16*d*	1/2	1/2	1/2	54(1)	U_{11}	U_{11}	−4(1)	U_{12}	U_{12}	54(1)
Al1	96*g*	0.05902(2)	*x*	0.32531(3)	110(1)	U_{11}	76(2)	−32(1)	−6(1)	U_{13}	99(1)
Al2	48*f*	0.48615(4)	1/8	1/8	81(2)	79(2)	U_{22}	0	0	−25(2)	80(1)
Al3	16*c*	0	0	0	193(2)	U_{11}	U_{11}	−39(2)	U_{12}	U_{12}	193(1)

Table 4: Interatomic distances (pm) in the structure of $Sr_{0.961(1)}V_2Al_{20}$. All distances of the first coordination spheres are listed. Standard deviations are all equal or less than 0.1 pm.

Sr:	4	Al3	317.0	Al2: 2	V	259.6
	12	Al1	324.8	2	Al1	272.0
V:	6	Al2	259.6	4	Al2	286.0
	6	Al1	282.2	4	Al1	287.0
Al1:	1	Al2	272.0	Al3:12	Al1	313.4
	1	Al1	274.7	2	Sr	317.0
	2	Al1	278.8			
	1	V	282.2			
	2	Al2	286.0			
	2	Al1	294.2			
	2	Al3	313.4			
	1	Sr	324.8			

with a modest increase of the lattice parameter with increasing x.[34] These phases have intensively been studied with respect to their low-temperature superconducting behavior and their low-energy rattling modes, which are a typical feature of cage compounds. It is a remarkable feature that the defect formation predominantly occurs for the 8*a* sites within the $[V_2Al_{20}]$ substructures. Although the $CeCr_2Al_{20}$ family of compounds is large, only few structures have been refined from precise single crystal diffraction data. Further data (refined occupancy parameters) is necessary in order to understand the origin of these homogeneity ranges.

For the crystal chemical discussion, we now focus on $Sr_{0.961(1)}V_2Al_{20}$. The unit cell and the coordination polyhedra are shown in Figure 1. The geometrical description is straightforward. The strontium and vanadium atoms build up a substructure that is equivalent to the cubic Laves phase $MgCu_2$. The aluminum atoms surround these sites. The larger strontium atoms have coordination number 16 and the smaller vanadium atoms coordination number 12, both forming Frank-Kasper type[35,36] polyhedra. Condensation of these two polyhedra types leads to a dense packing.

The shortest interatomic distances in the $Sr_{0.961(1)}V_2Al_{20}$ structure occur between the vanadium and aluminum atoms. The V–Al2 distance of 260 pm; however, is slightly longer than the sum of the covalent radii[37] of 247 pm for V + Al. This is comparable to aluminum-rich binary and ternary vanadium intermetallics, e. g., V_4Al_{23} (254–288 pm V–Al)[38] or $Yb_6V_4Al_{43}$ (253–284 pm V–Al).[39] The aluminum substructure of $Sr_{0.961(1)}V_2Al_{20}$ exhibits a broader range of Al–Al distances (272–313 pm). The three crystallographically independent aluminum atoms have between 10 and 12 aluminum neighbors. This is comparable to *fcc* aluminum (12 × 286 pm Al–Al).[40]

The important crystal chemical feature for the vanadium compounds is the vacancy formation on the 8*a* strontium site. The 16 aluminum neighbors of the strontium atoms have 4 × 317 pm Sr–Al3 and 12 × 325 pm Sr–Al1. These distances match with the sum of the covalent radii[37] of

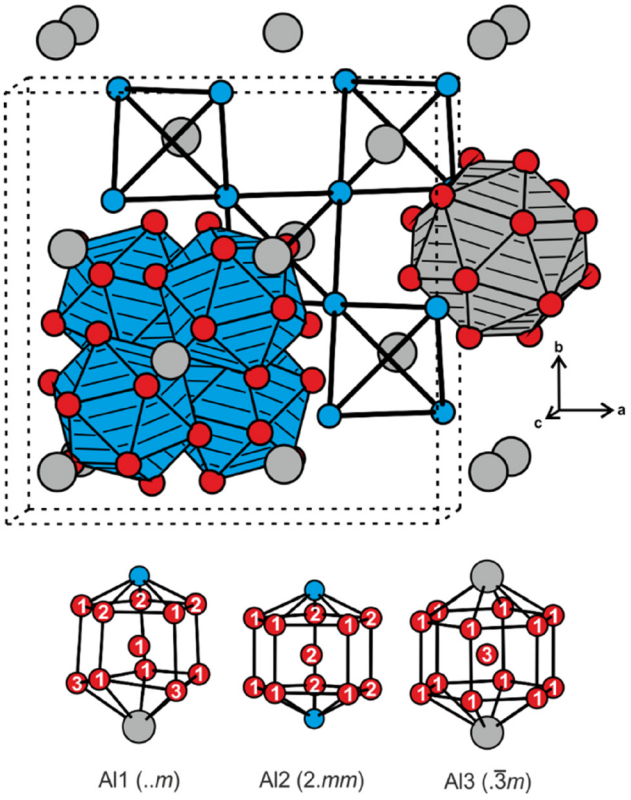

Figure 1: The crystal structure of $Sr_{0.961(2)}V_2Al_{20}$. The strontium, vanadium and aluminum atoms are shown as gray, blue and red circles, respectively. The top part of the figure shows the $MgCu_2$ substructure consisting of strontium and vanadium. The respective V@Al_{12} and Sr@Al_{16} coordination polyhedra are visualized as an example. The three crystallographically independent aluminum sites are shown on the bottom of the figure along with their site symmetry.

317 pm for Sr + Al. The Al3 atoms with the shorter Sr–Al distances directly react on the strontium defects and move towards the empty position. This is evident from the U_{11} displacement parameter which is enhanced in $Sr_{0.836(2)}V_2Al_{20}$ as compared to $Sr_{0.961(1)}V_2Al_{20}$.

3.2 Magnetic properties

Previous studies showed Curie-Weiss paramagnetism and antiferromagnetic ordering for $EuTi_2Al_{20}$ (T_N = 3.6 K)[15,17] and EuV_2Al_{20} (T_N = 5.5 K)[15,18] The antiferromagnetic ground states were corroborated by metamagnetic transitions in the 1.9 K magnetization isotherms.[15]

Here we studied the temperature dependent magnetic susceptibilities of the SrV_2Al_{20}, $Sr_{1.2}V_2Al_{20}$ and $SrTi_2Al_{20}$ samples (Figure 2). Down to 50 K the susceptibilities are almost temperature independent. The room temperature values

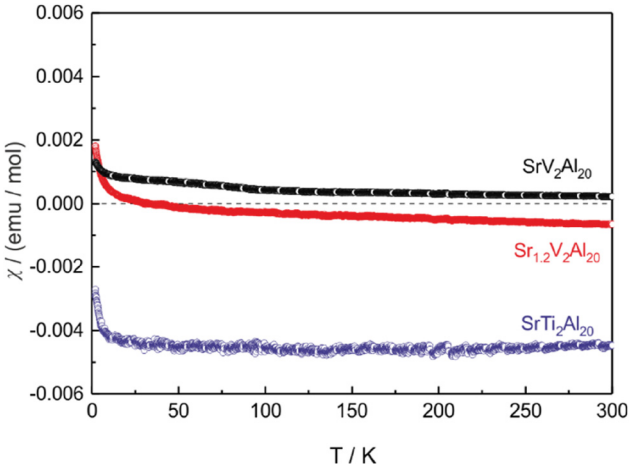

Figure 2: Temperature dependence of the magnetic susceptibility of the SrV_2Al_{20}, $Sr_{1.2}V_2Al_{20}$ and $SrTi_2Al_{20}$ samples measured at 10 kOe.

of $-4.4(1) \times 10^{-3}$ emu mol^{-1} ($SrTi_2Al_{20}$), $-6.4(1) \times 10^{-4}$ emu mol^{-1} ($Sr_{1.2}V_2Al_{20}$) and $2.2(1) \times 10^{-4}$ emu mol^{-1} (SrV_2Al_{20}) indicate diamagnetic, respectively Pauli paramagnetic behavior. In the case of the diamagnets, the intrinsic diamagnetism overcompensates the small Pauli contributions of these metals. Comparing the absolute values, $SrTi_2Al_{20}$ most likely has the smallest Pauli contribution. Below 50 K we observe slight increases of the susceptibilities, so-called Curie tails, which result from small amounts of paramagnetic impurities. It is worthwhile to note that a 20 Oe zero-field-colled/field-cooled measurement of the SrV_2Al_{20} sample showed a diamagnetic signal below 2 K. The Meissner part, however, was very low and this can be attributed to a tiny impurity phase.

Acknowledgements: We thank Dipl.-Ing. J. Kösters for the intensity data collections and help with the structure refinements.
Research ethics: Not applicable.
Informed consent: Not applicable.
Author contribution: All authors have accepted responsibility for the entire content of this submitted manuscript and approved the submission.
Use of Large Language Models, AI and Machine Learning Tools: Not relevant. Our group is able to think and act independently.
Conflict of interest: The authors declare no conflicts of interest regarding this article.
Research funding: This research was funded by Universität Münster and Deutsche Forschungsgemeinschaft (INST 211/1,034-1).
Data availability: Data is available from the corresponding author on well-founded request.

References

1. Nolas, G. S., Ed.; In *The physics and chemistry of inorganic clathrates*; Springer: Dordrecht, The Netherlands, 2014.
2. Remeika, J. P.; Espinosa, G. P.; Cooper, A. S.; Barz, H.; Rowell, J. M.; McWhan, D. B.; Vandenberg, J. M.; Moncton, D. E.; Fisk, Z.; Woolf, L. D.; Hamaker, H. C.; Maple, M. B.; Shirane, G.; Thomlinson, W. *Solid State Commun.* **1980**, *34*, 923–936.
3. Gumeniuk, R. Structural and physical properties of Remeika phases. In *Handbook on the Physics and Chemistry of Rare Earths*; Bünzli, J.-C. G., Kauzlarich, S. M., Eds.; North-Holland/Elsevier: Amsterdam, Chapter 304, Vol. 54, 2018; pp. 43–143. .
4. Krypyakevych, P. I.; Zarechnyuk, O. S. *Dopov. Akad. Nauk Ukr. RSR, Ser. A* **1968**, 364–367.
5. Pöttgen, R.; Janka, O. *Rev. Inorg. Chem.* **2023**, *43*, 357–383.
6. Villars, P.; Cenzual, K. *Pearson's Crystal Data - Crystal Structure Database for Inorganic Compounds*, Release 2024/25; ASM International: Materials Park, Ohio, USA, 2024.
7. Svanidze, E.; Kindly II, M.; Georgen, C.; Fulfer, B. W.; Lapidus, S. H.; Chan, J. Y.; Morosan, E. *J. Magn. Magn. Mater.* **2016**, *416*, 401–407.
8. Longworth, S. M.; Mou, M. M.; Yasmin, N.; Noor, M. F. B.; Sakidja, R.; Besara, T. *Crystals* **2025**, *15*, 391 (14 pages).
9. Yasmin, N.; Noor, M. F. B.; Besara, T. *J. Phys.: Condens. Matter* **2024**, *36*, 275801 (9 pages).
10. Schumacher, L.; Kösters, J.; Hensmann, L.; Pöttgen, R. *Z. Kristallogr.* **2024**, *239*, 367–376.
11. Schumacher, L.; Schreiner, F.; Koldemir, A.; Janka, O.; Hansen, M. R.; Pöttgen, R. *Dalton Trans.* **2025**, *54*, 8100–8112.
12. Shannon, R. D. *Acta Crystallogr.* **1976**, *A32*, 751–767.
13. Koldemir, A.; Klenner, S.; Pöttgen, R. *Z. Kristallogr. – N. Cryst. Struct.* **2023**, *238*, 507–509.
14. Niemann, S.; Jeitschko, W. *J. Solid State Chem.* **1995**, *114*, 337–341.
15. Ramesh Kumar, K.; Nair, H. S.; Christian, R.; Thamizhavel, A.; Strydom, A. M. *J. Phys.: Condens. Matter* **2016**, *28*, 436002 (14 pages).
16. Manyako, M. B.; Yahson, T. L.; Zarechnyuk, O. S. *Russ. Metall.* **1990**, *2*, 199–201.
17. Thiede, V. M. T.; Jeitschko, W.; Niemann, S.; Ebel, T. *J. Alloys Compd.* **1998**, *267*, 23–31.
18. Chi, J.; Li, Y.; Gou, W.; Goruganti, V.; Rathnayaka, K. D. D.; Ross, Jr., J. H. *Physica B* **2008**, *403*, 1426–1427.
19. Ramesh Kumar, K.; Nair, H. S.; Bhattacharyya, A.; Thamizhavel, A.; Strydom, A. M. *J. Magn. Magn. Mater.* **2018**, *452*, 205–209.
20. Kanatzidis, M. G.; Pöttgen, R.; Jeitschko, W. *Angew. Chem., Int. Ed.* **2005**, *44*, 6996–7023.
21. Yvon, K.; Jeitschko, W.; Parthé, E. *J. Appl. Crystallogr.* **1977**, *10*, 73–74.
22. Palatinus, L. *Acta Crystallogr.* **2013**, *69B*, 1–16.
23. Palatinus, L.; Chapuis, G. *J. Appl. Crystallogr.* **2007**, *40*, 786–790.
24. Petříček, V.; Dušek, M.; Palatinus, L. *Z. Kristallogr.* **2014**, *229*, 345–352.
25. Petříček, V.; Palatinus, L.; Plášil, J.; Dušek, M. *Z. Kristallogr.* **2023**, *238*, 271–282.
26. Hahn, T.; Klapper, H. Twinning of crystals. In *International Tables for Crystallography*; Authier, A., Ed., Vol. D, Chapter 3.3, Kluwer Academic Publishers, Dordrecht, The Netherlands, 2006.
27. Diamond, version 4.5, crystal impact, Bonn, Germany, 2018. http://www.crystalimpact.com.
28. CORELDRAW Graphics Suite 2023 (version 24.3.0.571), Corel Corporation: Ottawa, Ontario (Canada), 2023.
29. OriginPro 2024 (version 10.1.0.170), OriginLab Corporation, Nothhampton, Massachusetts (USA), 2024.
30. Higashinaka, R.; Nakama, A.; Ando, M.; Watanabe, M.; Aoki, Y.; Sato, H. *J. Phys.: Conf. Ser.* **2011**, *273*, 012033 (4 pages).
31. Doto, H.; Hirose, Y.; Honda, F.; Takeuchi, T.; Haga, Y.; Settai, R. *J. Alloys Compd.* **2017**, *693*, 332–338.
32. Gross, N.; Nasch, T.; Jeitschko, W. *J. Solid State Chem.* **2001**, *161*, 288–293.
33. Winiarski, M. J.; Griveau, J.-C.; Colineau, E.; Wochowski, K.; Wiśniewski, P.; Kaczorowski, D.; Caciuffo, R.; Klimczuk, T. *J. Alloys Compd.* **2017**, *696*, 1113–1119.
34. Hiroi, Z.; Onosaka, A.; Okamoto, Y.; Yamaura, J.-I.; Harima, H. *J. Phys. Soc. Jpn.* **2012**, *81*, 124707 (11 pages).
35. Frank, F. C.; Kasper, J. S. *Acta Crystallogr.* **1958**, *11*, 184–190.
36. Frank, F. C.; Kasper, J. S. *Acta Crystallogr.* **1959**, *12*, 483–499.
37. Emsley, J. *The Elements*; Oxford University Press: Oxford, 1999.
38. Smith, J. F.; Ray, A. E. *Acta Crystallogr.* **1957**, *10*, 169–172.
39. Wolff, M. W.; Niemann, S.; Ebel, T.; Jeitschko, W. *J. Magn. Magn. Mater.* **2001**, *223*, 1–15.
40. Donohue, J. *The Structures of the Elements*; Wiley: New York, 1974.